Eur. Phys. J. D **23**, 273–277 (2003)
DOI: 10.1140/epjd/e2003-00034-8

THE EUROPEAN PHYSICAL JOURNAL D

# High-Q whispering gallery modes in a spherical shell dielectric resonator: Characterization at microwave frequencies

I. Longo[1,a], D. Cros[2], and N. Tosoratti[1]

[1] Institute for Chemical-Physical Processes, CNR, Via G. Moruzzi 1, 56124 Pisa, Italy
[2] IRCOM[b], U.F.R. des Sciences, Universit de Limoges, 87060 Limoges Cedex, France

Received 25 October 2002
Published online 4 February 2003 – 

**Abstract.** We present a numerical and experimental characterization of high-$Q$ whispering gallery resonant modes excited in a fused quartz spherical shell operated in the 18–26.5 GHz band; easy coupling and selection of modes is a most advantageous feature of the proposed structure with respect to ordinary bulk resonators. The numerical results, based on a finite element algorithm, well match experimental data, which also show the capability of our device to perform gaseous spectroscopy measurements.

**PACS.** 41.20.Jb Electromagnetic wave propagation; radiowave propagation

## 1 Introduction

In the late 30's Ritchmeyer showed that spherical shaped open dielectric structures support high-$Q$ *whispering gallery* (WG) resonant modes thanks to the total reflection of the electromagnetic (EM) field at the curved dielectric-air interface [1]. Later experimental works confirmed that the $Q$ factors exhibited by WG modes almost reach the limit imposed by the intrinsic material losses, that is $Q_{\max} = \varepsilon'/\varepsilon'' = (\tan\delta)^{-1}$, where $\varepsilon = \varepsilon' + \mathrm{i}\varepsilon''$ and $\tan\delta$ denote, respectively, the complex permittivity and the loss tangent of the dielectric material at the operating frequency.

Recent studies have focussed on WG modes in fused silica spheres at optical frequencies: $Q$ factors of the order of $10^8$ were observed in microspheres at infrared frequencies and at room temperature [2]. The bare use of a laser beam to excite WG modes at optical frequencies in a spherical dielectric resonator with diameter much larger than the working wavelength proves ineffective, as the beam cannot be confined into the resonator without resorting to a mode matching device. A good coupling may be attained exploiting the evanescent field generated by an optical fiber tangent to the resonator surface [3], or using a frustrated total internal reflection prism [2].

In this work we examine a new resonant structure formed by a thin spherical dielectric shell instead of a bulk sphere, which allows direct laser coupling of the WG modes: the incident laser beam, once refracted through the external surface of the shell, undergoes total reflection at the inner dielectric-air interface and is eventually trapped in the shell. The same effect is observed when a beam of visible laser radiation impinges tangentially on the surface of a transparent light bulb or of a glass tube. Easy WG modes coupling, not needing optical fibers or prisms, is thus a remarkably attractive feature of the proposed *spherical shell dielectric resonator* (SSDR). We verified that a similar behaviour shows at microwave frequencies too, upon proper rescaling of the resonator. Namely, we tested the electromagnetic response in the 18–26.5 GHz band of an SSDR prototype made in fused quartz. Experimental results were compared with the predictions of numerical calculations based on a finite element algorithm: a good agreement was found between measured and calculated $Q$s and resonant frequencies of the WGH modes supported by our SSDR, *i.e.* WG modes with magnetic flux lines lying in the plane located by the resonator radius and the wave vector. We also verified that WGH modes may be excited through direct exposure of the SSDR to the far field of a radiating antenna and tested the capability of our device to perform gaseous spectroscopy measurements exploiting the evanescent field just outside the inner surface of the dielectric shell: note that a full dielectric sphere would not allow the latter type of measurements.

## 2 The resonant structure

The SSDR prototype we examined both numerically and experimentally is sketched in Figure 1. It was made out of a 250 ml commercial fused quartz flask, with 85 mm diameter and $1.7\pm0.2$ mm thickness (nominal values), and was endowed with a single female 29/32 conical neck ($N$); a vacuum port ($VM$) on $N$ connected the resonator to a

[a] e-mail: longo@ifam.pi.cnr.it
[b] U.A. CNRS 356

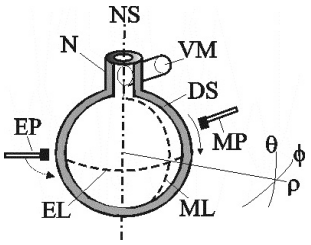


**Fig. 1.** Schematic representation of our fused quartz flask resonator: $DS$ = dielectric shell; $N$ = female 29/32 conical neck; $VM$ = vacuum port; $EL$ and $ML$ = equatorial and meridian lines; $NS$ = north-south axis; $EP$ and $MP$ = equatorial and meridian perturbing probes.

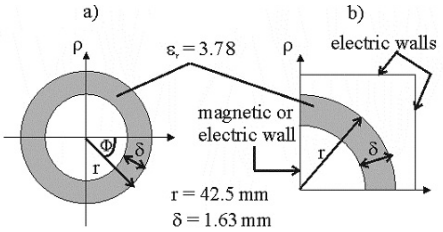


**Fig. 2.** (a) Cross-section of the real resonating structure; (b) cross-section of the virtual device used for numerical calculations.

standard high-vacuum manifold. Low dielectric losses and a regular geometrical shape were key factors in choosing the flask among many available samples.

It proves useful to describe our structure in geographical terms, locating equatorial and meridian lines on the resonator surface ($EL$ and $ML$, respectively) and referring to the axis of symmetry of the flask as north-south ($NS$) axis. Since WG modes mainly propagate along the equatorial belt, geometrical imperfections in the polar regions have little effect: therefore, the presence of the neck at the top of the flask and, possibly, of a flat bottom do not affect the EM response of the device.

## 3 Finite element analysis

The finite element method used to calculate the resonant frequencies and the EM parameters of the SSDR described above makes use of a mixed solution obtained with Nedelec and Lagrange's second-order polynomial interpolation, which does not introduce any spurious solution: details are available in reference [4]. The numerical analysis of our device requires proper shielding with electric and/or magnetic walls; besides, due to the spherical symmetry, only a quarter of the structure needs to be considered: in Figure 2 the cross-sections of the real device and of the virtual device used for numerical computation are compared.

Calculations were made assuming that the inner and outer surfaces of the shell are perfectly spherical and concentric and that the relative complex dielectric permittivity of quartz is: $\varepsilon = 3.78 - \mathrm{i}\,3.78 \times 10^{-4}$ (which corresponds to: $\tan\delta = 10^{-4}$) throughout the explored frequency band.

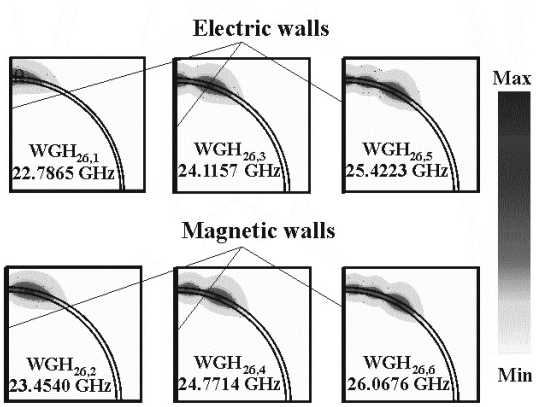


**Fig. 3.** Electric field distribution inside and close to the dielectric shell calculated for modes $\mathrm{WGH}_{26,m}$ with low $m$ values.

If necessary, the same finite element algorithm may also take into account losses due to isotropic/anisotropic dielectric/magnetic material and to metallic walls. Solving in two dimensions yields resonant frequencies, unloaded quality factors and field cartography for $\mathrm{WGH}_{n,m}$ modes of our SSDR; indexes $n$ and $m$ describe the periodicity of the EM field distribution, the former with respect to the azimuth angle $\phi$ and the latter with respect to the meridian angle $\theta$ in a spherical system of coordinates $\{\rho, \phi, \theta\}$. A third index $l$ related to the field periodicity in radial direction should also be considered, but it may be omitted in our case, as the thickness of the shell is smaller than the radiation wavelength so that $l = 1$ for all modes.

Figure 3 shows the distribution of the electric field amplitudes relative to modes with equatorial index $n = 26$ and compatible with the presence of an electric wall (odd $m$ index) or a magnetic wall (even $m$ index); the magnetic field amplitudes exhibit analogous distributions. Table 1 reports the calculated resonant frequencies of several $\mathrm{WGH}_{n,m}$ modes compared to measured values: an excellent agreement was found.

For each detected resonance of the real device the measured values of modal indexes $n$ and $m$ turned out to be exactly those reported in the first column of Table 1 and used for numerical calculations relative to the virtual device of Fig. 2b).

## 4 Measurement line and techniques

### 4.1 Experimental set-up

Figure 4 is a sketch of the experimental set-up used for K-band measurements on our SSDR. The microwave source was a swept oscillator ($SO$), feeding a dielectric rod waveguide ($DR$) almost tangential to the equatorial line of the resonator: WG modes in the SSDR were excited by the evanescent field just outside $DR$. Power was sent to $DR$ through a standard rectangular $\mathrm{TE}_{10}$ waveguide ($SW$), followed by a ferrite uniline ($U$, which suppressed reflected waves) and by a variable attenuator ($VA$, which adjusted the signal level); the connection to $DR$ was made through

**Table 1.** Calculated and measured resonant frequencies.

| Modal indexes $(n, m)$ | Calculated frequencies (MHZ) | Measured frequencies (MHZ) | Relative error (%) |
|---|---|---|---|
| (20, 1) | 18 637.9 | 18 616.0 | 0.11 |
| (21, 1) | 19 374.4 | 19 330.0 | 0.23 |
| (22, 1) | 20 049.5 | 20 055.0 | 0.030 |
| (23, 1) | 20 744.1 | 20 760.0 | 0.077 |
| (24, 1) | 21 431.7 | 24 443.0 | 0.056 |
| (25, 1) | 22 122.4 | 22 131.8 | 0.040 |
| (26, 1) | 22 786.5 | 22 807.4 | 0.092 |
| (27, 1) | 23 454.5 | 23 489.0 | 0.15 |
| (28, 1) | 24 116.6 | 24 142.1 | 0.10 |
| (29, 1) | 24 773.2 | 24 794.4 | 0.080 |
| (30, 1) | 25 424.6 | 25 444.4 | 0.079 |
| (31, 2) | 26 071.1 | 26 087.1 | 0.060 |
| (23, 2) | 21 431.1 | 21 627.5 | 0.90 |
| (24, 2) | 22 120.0 | 22 312.8 | 0.86 |
| (25, 2) | 22 786.1 | 22 990.0 | 0.89 |
| (26, 2) | 23 454.1 | 23 668.5 | 0.90 |
| (27, 2) | 24 116.2 | 24 328.0 | 0.87 |
| (28, 2) | 24 772.8 | 24 990.5 | 0.87 |
| (29, 2) | 25 424.1 | 25 645.5 | 0.86 |
| (30, 2) | 26 070.7 | 26 283.0 | 0.81 |
| (25, 3) | 23 453.7 | 23 000.5 | 1.9 |
| (26, 3) | 24 115.7 | 24 452.0 | 1.3 |
| (27, 3) | 24 772.3 | 25 117.6 | 1.3 |
| (28, 3) | 25 423.6 | 25 777.4 | 1.4 |
| (25, 4) | 24 115.0 | 24 509.0 | 1.6 |
| (27, 4) | 25 422.7 | 25 848.0 | 1.6 |
| (24, 5) | 24 114.0 | 24 422.0 | 1.2 |

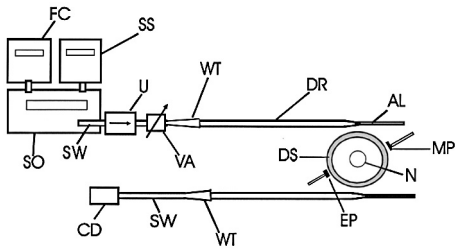


**Fig. 4.** A schematic representation of the experimental apparatus: $SO$ = sweep oscillator; $SW$ = standard rectangular waveguide; $FC$ = frequency counter; $SS$ = source synchronizer; $U$ = ferrite uniline; $VA$ = variable attenuator; $WT$ = rectangular to circular waveguide transition; $DR$ = dielectric rod; $AL$ = absorbing line (see also Fig. 5); $CD$ = crystal detector.

a rectangular to circular waveguide transition ($WT$). Another $DR$ (on the opposite side of the resonator) picked up the power transmitted through the SSDR, delivering it to a crystal mixer-detector ($CD$, type 1N26). Tuning and detection of the actual operating frequency were performed by a source synchronizer ($SS$) and a frequency counter ($FC$), while a digital oscilloscope and a plotter (not shown in Fig. 4) visualized and recorded the SSDR output signal.

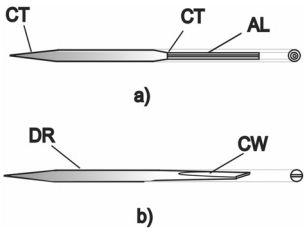


**Fig. 5.** Two alternative designs for the dielectric rods of Figure 4: (a) rod with both ends tapered ($CT$): the left end fitted into $WT$ (not shown), while the other was soldered to a second rod, properly coated to enhance microwave absorption (absorbing line, $AL$); (b) rod with only one end tapered, the other being shaped as a wedge ($CW$).

### 4.2 Coupling elements design and realization

Figure 5 shows two different realizations of the $DR$s used to couple power in and out of the SSDR.

In Figure 5a is a fused quartz rod with tapered ends ($CT$): the taper facilitated insertion of $DR$ in $WT$, while a few turns of thin PTFE tape wrapped around the rod close to the taper eliminated residual clearances; at the opposite end the rod was soldered to a thin fused quartz tube ($AL$), coated with colloidal graphite in order to maximize microwave absorption and avoid reflections. In the alternative design of Figure 5b the conical taper was substituted at one end by a wedge ($CW$, modelled with a grinding machine), which proved very useful for mode tuning: indeed, optimal coupling conditions for a particular group of modes was attained through slight adjustments of the orientation of the wedge plane with respect to the SSDR north-south axis.

### 4.3 Measurement technique

The experimental evaluation of the azimuthal index $n$ of a well isolated resonance was performed by first tuning the source on the corresponding peak in the frequency response of the resonator and then recording the variations in the signal transmitted through the SSDR as a small perturbing probe ($EP$ in Figs. 1 and 4) was slowly displaced along the equatorial line of the device, about 3 mm distant from its surface. Modal index $m$ values, instead, were measured by moving another small probe ($MP$ in Fig. 1) along a meridian line of the resonator, placed at about 1 mm from the outer surface of the shell: $m$ equalled the number of sharp decreases observed in the transmitted signal as $MP$ was displaced from north to south pole of the SSDR. The meridian probe $MP$ was made out of a 3 mm graphite lump, while the equatorial probe $EP$ was a thin metal rod about 5 mm long and 0.8 mm wide, lying almost parallel to the electric field lines of the WG mode under investigation; both probes were glued on the tip of a 1 mm fused quartz rod attached to a motor driven rotating frame (not shown in Fig. 1). This measurement technique is more accurately described in reference [5].

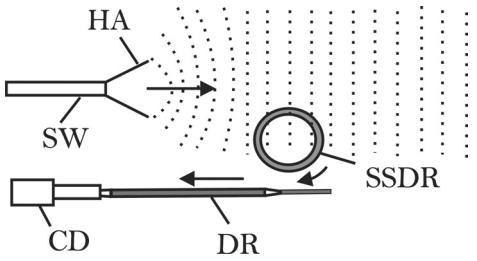


**Fig. 6.** Excitation of the WGH modes of our SSDR through a horn pyramidal antenna ($HA$) radiating a quasi-plane wave with electric field perpendicular to the equatorial plane of the resonator.

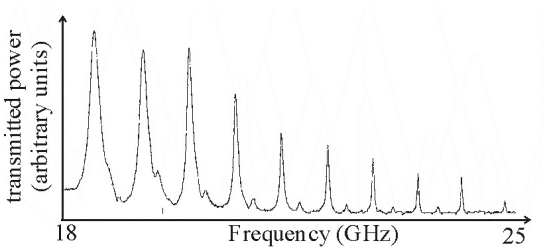


**Fig. 7.** Crystal video detection of the frequency response of our resonator excited with the technique shown in Figure 6. Each peak locates a different $\mathrm{WGH}_{n,m}$ resonance.

## 5 Experimental results

### 5.1 Excitation of WGH resonances and Q measurements

In the first place, we verified that the WGH modes of our SSDR may be directly excited by the quasi-plane wave produced by a pyramidal horn antenna ($HA$) placed several centimetres away from the resonator, the associated electric field being perpendicular to the equatorial plane of the device (see Fig. 6): such an experimental set-up is the microwave equivalent of direct laser excitation of an optical resonator. Figure 7 reports the crystal video detection of WGH resonances coupled by $HA$ in the 18–25 GHz band: these results clearly prove the feasibility of direct coupling.

However, the transmission scheme of Figure 4 provided a better and more selective coupling of the resonant modes: with the latter set-up, the voltage signal output by the crystal detector $CD$ and visualized by the oscilloscope exhibited undercoupled peaks of about 100 mV on a nearly flat zero baseline; moreover, absorption measurements (performed with the same set up, but using just one dielectric rod) showed that more than 90% of the power output by the microwave source is actually coupled to the resonant modes with this method of excitation. For all measurements presented hereafter we resorted to the $DR$ evanescent field coupling technique of Figure 4.

The frequencies and the $Q$ factors of the WG resonances were measured by sweeping the synchronized microwave source $SO$ over a few MHz wide band: a typical video detection relative to a single frequency sweep appears in Figure 8. Peak detection in the frequency response of our resonator was within a 0.5 MHz uncertainty margin, mainly due to temperature and humidity variations in the lab and on the SSDR surface and to perturbations induced by the operator's presence and movements in proximity of the open dielectric structure. By varying the distance between the exciting $DR$ and the resonator surface and by moving the tip of the rod both in radial direction and along a meridian line, it was possible to couple selected families of resonant modes, with index $n$ in the range 20–30 and index $m$ being a fixed small integer.

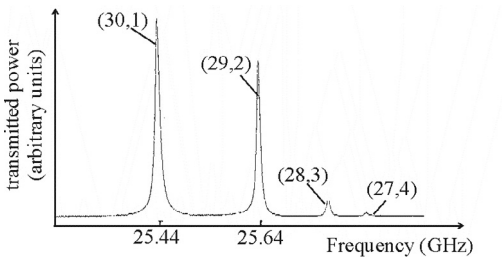


**Fig. 8.** $\mathrm{WGH}_{n,m}$ resonances detected in a single frequency sweep. From left to right: $(n,m) = (30,1)$, $(29,2)$, $(28,3)$ and $(27,4)$. The decreasing amplitude is due to the angular distribution of the EM field.

Unloaded $Q$ factors were measured in low coupling conditions, keeping the crystal detector $CD$ in the square region of its characteristic curve. The relative uncertainty on $Q$ measurements turned out to be 10% at most, depending on the signal level and on the possible presence of other nearby resonances.

The measured $Q$ factors of the WGH resonances ranged from a few hundred for modes in the 18–20 GHz band ($Q > 10^3$ only for $n > 24$) up to a maximum of $7\,300 \pm 300$ recorded for the $\mathrm{WGH}_{30,1}$ mode, resonating at 25.44 GHz; the latter value is readily comparable to that calculated with the finite element algorithm, namely:

$$Q_{30,1} = (\alpha_{30,1} \tan\delta)^{-1} = \begin{cases} 12\,617.7, & \text{with} \quad \tan\delta = 10^{-4} \\ & \text{(nominal loss tangent)} \\ 7\,422.1, & \text{with} \quad \tan\delta = 1.7 \times 10^{-4} \\ & \text{(effective loss tangent)} \end{cases} \tag{1}$$

$\alpha_{30,1}(\approx 0.79)$ being the *electric ratio* relative to the $\mathrm{WGH}_{30,1}$ mode, *i.e.* the ratio between the electric energy stored in the dielectric shell and the total electric energy, including that stored in the evanescent field which decays exponentially with increasing distance from the dielectric surface. As shown in (1), matching measured and calculated $Q$ factors requires the use of an effective loss tangent, of the same order but greater than the nominal value found in literature for quartz at K-band frequencies: indeed, radiative losses and other non ideal behaviours not accounted for in the numerical model produce the same net effect as an increase in the loss tangent of the dielectric shell.

### 5.2 Frequency shift under vacuum conditions and gaseous spectroscopy

Finally, we tested the high vacuum response of the SSDR and verified its capability to perform gaseous spectroscopy measurements. To this end the SSDR was connected through the vacuum port $VM$ in its neck $N$ (see Fig. 1) to a vacuum and gas handling manifold. Pumping air out of the SSDR slightly lowered the resonant frequencies; in particular, the measured shift for the $WGH_{28,1}$ mode was:

$$\Delta\nu = \nu_{\rm air} - \nu_{\rm vac} = 1.0 \pm 0.1 \text{ MHZ} \qquad (2)$$

where $\nu_{\rm air} = 24\,142$ MHz is the $WGH_{28,1}$ resonant frequency recorded when both surfaces of the dielectric shell were exposed to ambient pressure and $\nu_{\rm vac} = 24\,141$ MHz was the value recorded in high vacuum. The frequency shift is due to the evanescent EM field decaying exponentially just outside the inner surface of the resonator, the rate of decay depending on the permittivity of the surrounding fluid.

The resonant frequency of the $WGH_{28,1}$ mode was very close to the peak frequency of the (4–4) $N^{14}H_3$ inversion line, namely 24 139.45 MHz [6]. Thus, upon producing high vacuum inside the SSDR, we introduced in it a controlled quantity of ammonia and exploited the evanescent EM field in proximity of the inner surface of the dielectric shell to perform spectroscopic measurements. The fine frequency tuning of the $WGH_{28,1}$ resonance onto the peak resonant frequency of the (4–4) ammonia inversion line was obtained using a 4 cm wide and 1 mm thick PTFE slab displaced in the equatorial plane in proximity of the external SSDR surface by a precision mechanism. With this tuning technique the resonant frequency could be lowered up to a maximum of 2 MHz without appreciably affecting the $Q$ factor of the resonance.

The ammonia inversion linewidth is $LW = 24.4$ MHz/torr [7], while the bandwidth of the SSDR resonance is about 8 MHz: therefore, clearly visible absorption dips may be obtained only for ammonia pressures $\ll 0.3$ torr. Figure 9 displays the measured frequency dependence of the power transmitted by the SSDR at three different ammonia pressures, namely: $P_1 \sim 2 \times 10^{-2}$ torr (squares), $P_2 \sim 1.5 \times 10^{-2}$ torr (circles) and $P_3 \sim 10^{-3}$ torr (triangles), the latter experimental curve showing a residual wall degassing. The ammonia absorption peak was maximized by attenuating the microwave source power level down to $-1$ dBm, so as to prevent power saturation phenomena [6]. These results clearly show that our SSDR may be usefully employed for gaseous spectroscopy in the evanescent field.

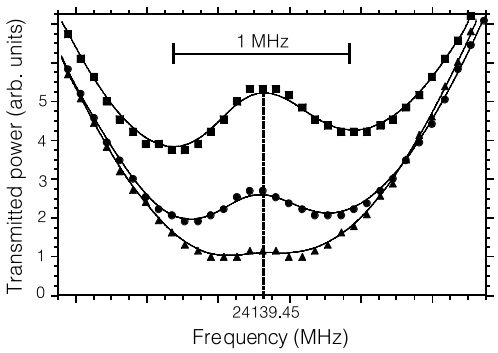


**Fig. 9.** Crystal video detection of the power transmitted by our SSDR, tuned on the $NH_3$ (4–4) inversion line (24 139.45 MHz), as a function of frequency. The resonator was filled with ammonia at three different pressures: $P_1 \sim 2 \times 10^{-2}$ torr (squares), $P_2 \sim 1.5 \times 10^{-2}$ torr (circles) and $P_3 \sim 10^{-3}$ torr (triangles).

## 6 Conclusion

We presented a numerical and experimental characterization of a family of high-$Q$ whispering gallery resonant modes supported by a resonator of new design, consisting of a spherical dielectric shell. The finite element algorithm used to calculate the resonant frequencies, the $Q$ factors and the field distributions of the whispering gallery modes yields results in good agreement with experimental data, collected at microwave frequencies using a prototypal resonator made out of a fused quartz flask. Direct excitation of the modes through the bare use of a radiating antenna was shown to be feasible: easier mode coupling with respect to ordinary bulk dielectric resonators is thus a most attractive feature of the proposed structure.

A comparison between the maximum theoretical $Q$ factor and the highest $Q$ value actually measured proves that the electromagnetic field is pretty well confined in the device. Moreover, the amplitude of the evanescent electric field just outside the inner surface of the resonator is rapidly decaying but still sufficiently high to allow for experiments of gaseous spectroscopy, as demonstrated by measuring the (4–4) ammonia inversion line.

The proposed spherical shell dielectric resonator appears to be a good candidate for the construction of a new class of high-$Q$ optical micro-resonators.

## References

1. R.D. Richtmeyer, J. Appl. Phys. **10**, 391 (1939)
2. V.B. Braginsky, M.L. Gorodetsky, V.S. Ilchenko, Phys. Lett. A **137**, 393 (1989)
3. J.C. Knight, G. Cheung, F. Jaques, T.A. Birks, Opt. Lett. **22**, 1129 (1997)
4. M. Aubourg, P. Guillon, J. Electromagn. Waves Appl. **5**, 371 (1991)
5. I. Longo, Meas. Sci. Technol **2**, 1169 (1991)
6. P. Kisliuk, C.H. Townes, *Molecular Microwave Spectra Tables* (NBS Research paper N RP2107, 1950), Vol. 44, p. 625
7. R.L. Legan, J.A. Roberts, E.A. Rinehart, C.C. Lin, J. Chem. Phys. **43**, 4337 (1965)